Geophysical Prospecting

EAGE EUROPEAN ASSOCIATION OF GEOSCIENTISTS & ENGINEERS

Geophysical Prospecting, 2019, **67**, 2343–2357 doi: 10.1111/1365-2478.12821

Source-independent waveform inversion for attenuation estimation in anisotropic media

Tong Bai* and Ilya Tsvankin

Center for Wave Phenomena, Colorado School of Mines, Golden, CO 80401, USA

Received January 2019, revision accepted May 2019

ABSTRACT

In previous publications, we presented a waveform-inversion algorithm for attenuation analysis in heterogeneous anisotropic media. However, waveform inversion requires an accurate estimate of the source wavelet, which is often difficult to obtain from field data. To address this problem, here we adopt a source-independent waveform-inversion algorithm that obviates the need for joint estimation of the source signal and attenuation coefficients. The key operations in that algorithm are the convolutions (1) of the observed wavefield with a reference trace from the modelled data and (2) of the modelled wavefield with a reference trace from the observed data. The influence of the source signature on attenuation estimation is mitigated by defining the objective function as the ℓ_2-norm of the difference between the two convolved data sets. The inversion gradients for the medium parameters are similar to those for conventional waveform-inversion techniques, with the exception of the adjoint sources computed by convolution and cross-correlation operations. To make the source-independent inversion methodology more stable in the presence of velocity errors, we combine it with the local-similarity technique. The proposed algorithm is validated using transmission tests for a homogeneous transversely isotropic model with a vertical symmetry axis that contains a Gaussian anomaly in the shear-wave vertical attenuation coefficient. Then the method is applied to the inversion of reflection data for a modified transversely isotropic model from Hess. It should be noted that due to the increased nonlinearity of the inverse problem, the source-independent algorithm requires a more accurate initial model to obtain inversion results comparable to those produced by conventional waveform inversion with the actual wavelet.

Key words: Anisotropy, Attenuation, Elastics, Full-waveform inversion.

1 INTRODUCTION

Seismic data are substantially influenced by intrinsic attenuation in the subsurface. The loss of high frequencies in attenuative media reduces the bandwidth of the recorded wavefields and, therefore, the resolution of seismic inversion and imaging. Reliable estimation of attenuation and compensation for its influence can improve the output of many seismic processing steps including amplitude-variation-with-offset analysis and imaging (e.g. Zhu, Harris and Biondi 2014; Bai, Zhu and Tsvankin 2019). In addition, attenuation coefficients can be employed in reservoir characterization because they provide information for fracture and fluid detection and for estimation of permeability (Donald, Butt and Iakovlev 2004; Carcione, Morency and Santos 2010; Müller, Gurevich and Lebedev 2010).

Subsurface formations that exhibit velocity anisotropy are often characterized by directionally dependent attenuation coefficients (Zhu *et al.* 2006; Best, Sothcott and McCann 2007). In particular, numerical and laboratory experiments

*E-mail: tbai@mines.edu

have confirmed the link between attenuation anisotropy and parameters of aligned fractures (Rao and Wang 2009; Ekanem *et al.* 2013; Guo and McMechan 2017). To characterize the anisotropic attenuation coefficients of P- and SV-waves in thinly layered porous rocks, Krzikalla and Müller (2011) combine anisotropic Backus limits (under quasi-static and no-flow assumptions) with interlayer flow models.

The quality factor, which is responsible for attenuation, is often estimated by the frequency-shift and spectral-ratio methods based on the frequency dependence of attenuation coefficients (e.g. Quan and Harris 1997; Sams and Goldberg 1990). However, these methods suffer from high sensitivity to noise and to event interference and are difficult to apply to realistic heterogeneous models (de Castro Nunes *et al.* 2011).

A viable alternative to the conventional techniques is waveform inversion (WI), which is often used in high-resolution velocity analysis (e.g. Tarantola 1984, Plessix *et al.* 2013). The influence of attenuation on both the amplitude and phase of seismic waves makes it an essential component of WI. Proper compensation for attenuation can significantly increase the accuracy of the estimated velocity parameters (Causse, Mittet and Ursin 1999; Kurzmann *et al.* 2013; Xue *et al.* 2016). Some existing algorithms adopt a hierarchical strategy, in which velocity analysis is followed by attenuation estimation (Kamei and Pratt 2008; Prieux *et al.* 2013). Other implementations of WI for attenuative media rely on a priori knowledge of the velocity parameters (Bai and Yingst 2013; Bai, Tsvankin and Wu 2017).

Errors in the source wavelet represent a serious challenge in application of WI. Luo, Yuan and Wang (2014) demonstrate that an inaccurate wavelet phase may substantially distort the inverted velocity field. Using modelled elastic data for shallow subsurface, Groos *et al.* (2014) show that a properly designed source-wavelet correction can simulate most of the observed viscoelastic effect, which indicates a significant cross-talk between the source signature and attenuation parameters.

There are two main strategies to account for the influence of the source wavelet: joint inversion for the source signal and medium parameters (Wang *et al.* 2009; Sun *et al.* 2014) and so-called source-independent waveform inversion (SIWI) (Choi and Alkhalifah 2011; Shigapov *et al.* 2013). Due to the trade-offs between the source signature and attenuation, SIWI is better suited for attenuation analysis. Shigapov *et al.* (2013) compare three types of source-independent misfit functions in the frequency domain designed to remove the influence of the source wavelet from attenuation estimation. Their synthetic test for microseismic and crosswell data from a layered isotropic viscoelastic medium shows that the best inversion results are obtained with the convolution-based objective function. In the time domain, a source-independent objective function is introduced for acoustic media by Choi and Alkhalifah (2011) and for elastic isotropic models by Zhang *et al.* (2016).

In the framework of the generalized standard linear solid model, Bai and Tsvankin (2016) develop a time-domain finite-difference modelling algorithm for anisotropic attenuative media, which produces nearly frequency-independent elements Q_{ij} of the quality-factor matrix. Employing that simulator, Bai *et al.* (2017) design a time-domain WI methodology for estimation of the attenuation parameters of VTI (transversely isotropic with a vertical symmetry axis) media. The gradients of the objective function are computed using the adjoint-state method. The four Thomsen-style parameters (Zhu and Tsvankin 2006) describing the attenuation of P- and SV-waves are updated simultaneously. The influence of velocity errors is mitigated by employing the local-similarity technique (Fomel 2009).

Here, we incorporate the time-domain source-independent objective function proposed by Choi and Alkhalifah (2011) into the viscoelastic WI algorithm of Bai *et al.* (2017). First, we briefly review the methodology of time-domain modelling and waveform inversion in anisotropic attenuative media. Next, we introduce the source-independent WI objective function and the corresponding adjoint sources. To reduce the influence of errors in the velocity parameters on the inversion results, we integrate the local-similarity method into SIWI. Finally, synthetic tests confirm the ability of the developed methodology to estimate the VTI attenuation parameters without knowledge of the source signature.

2 METHODOLOGY

2.1 Forward modelling for viscoelastic anisotropic media

We simulate wave propagation in viscoelastic VTI (transversely isotropic with a vertical symmetry axis) media with a time-domain finite-difference code described in Bai and Tsvankin (2016). To increase computational efficiency, only one relaxation mechanism is employed, which is generally sufficient for nearly constant-Q simulation within the frequency band typical for seismic surveys (Zhu, Carcione and Harris 2013).

The relaxation function for arbitrarily anisotropic attenuative media can be found in Bai and Tsvankin (2016). For a

single relaxation mechanism, that function has the form (no index summation is assumed):

$$\Psi_{ijkl}(t) = C^R_{ijkl}\left(1 + \tau_{ijkl}\, \mathrm{e}^{-t/\tau^\sigma}\right) H(t), \tag{1}$$

where $C^R_{ijkl} = \Psi_{ijkl}(t \to \infty)$ is called the 'relaxed stiffness,' τ^σ denotes the stress relaxation time determined by the reference frequency (frequency at which velocity and attenuation parameters are defined), the parameters τ_{ijkl} control the difference between the stress and strain relaxation time (and, therefore, they determine the magnitude of attenuation in anisotropic media), and $H(t)$ is the Heaviside function. At zero time, the relaxation function generates the 'unrelaxed stiffnesses' C^U_{ijkl}:

$$C^U_{ijkl} \equiv \Psi_{ijkl}(t = 0) = C^R_{ijkl}(1 + \tau_{ijkl}). \tag{2}$$

The stiffness difference $\Delta C_{ijkl} = C^U_{ijkl} - C^R_{ijkl}$, which depends on τ_{ijkl}, quantifies the magnitude of attenuation.

The P- and SV-wave attenuation in VTI media is conveniently described by the Thomsen-style parameters A_{P0}, A_{S0}, ε_Q and δ_Q (Zhu and Tsvankin 2006; Bai and Tsvankin 2016). A_{P0} and A_{S0} are the vertical (symmetry-axis) P- and S-wave attenuation coefficients, the parameter ε_Q depends on the fractional difference between the P-wave attenuation coefficients in the horizontal and vertical directions and δ_Q controls the curvature of the P-wave attenuation coefficient at the symmetry axis. The explicit expressions for these parameters in terms of the real-valued stiffnesses and elements of the quality-factor matrix can be found in Zhu and Tsvankin (2006). Combined with the unrelaxed stiffness coefficients C^U_{ijkl} (used as the reference elastic parameters), the Thomsen-style attenuation parameters can be converted into the quality-factor elements Q_{ijkl} or the stiffness differences ΔC_{ijkl}.

The time-domain viscoelastic stress (σ_{ij})–strain(ϵ_{kl}) relationship can be written as

$$\sigma_{ij} = C^U_{ijkl}\,\epsilon_{kl} + \Delta C_{ijkl}\, r_{kl}, \tag{3}$$

where r_{kl} are the memory variables, which satisfy the following partial differential equations (Bai and Tsvankin 2016):

$$\frac{\partial r_{kl}}{\partial t} = -\frac{1}{\tau^\sigma}(r_{kl} + \epsilon_{kl}). \tag{4}$$

2.2 Viscoelastic waveform inversion for anisotropic media

The quality of data fitting during the model-updating process is often measured by the ℓ_2-norm objective function (e.g. Tarantola 1988; Tromp, Tape and Liu 2005):

$$F(\mathbf{m}) = \frac{1}{2} \parallel \mathbf{u}(x_r, t, \mathbf{m}) - \mathbf{d}(x_r, t) \parallel^2, \tag{5}$$

where $\mathbf{u}(x_r, t, \mathbf{m})$ and $\mathbf{d}(x_r, t)$ are the simulated and observed data, respectively, $\mathbf{m}$ is the vector of model parameters and t is the time. Summation over shots and receivers is implied. By applying the adjoint-state method (Tarantola 1988; Tromp *et al.* 2005; Fichtner 2005), the gradient of the objective function at each iteration is obtained from only two wavefield simulations (one forward and one adjoint). The gradients for the viscoelastic parameters ΔC_{ijkl} can be computed in the Born approximation as the cross-correlation of the adjoint strain field with the memory variables from the forward simulation (Tarantola 1988; Bai *et al.* 2017):

$$\frac{\partial F}{\partial \Delta C_{ijkl}} = -\int_0^T \frac{\partial u^\dagger_i}{\partial x_j}\, r_{kl}\, dt, \tag{6}$$

where $\mathbf{u}^\dagger$ denotes the adjoint displacement field and T is the recording time.

Following Bai *et al.* (2017), the inversion algorithm for VTI models operates with the vertical P- and S-wave attenuation coefficients introduced above (A_{P0} and A_{S0}), the P-wave horizontal attenuation coefficient A_{Ph},

$$A_{Ph} = (1 + \varepsilon_Q)\, A_{P0} \approx \frac{1}{2\,Q_{11}}, \tag{7}$$

and the coefficient A_{Pn}, which governs the angular variation of the P-wave attenuation near the symmetry axis:

$$A_{Pn} = (1 + \delta_Q)\, A_{P0}. \tag{8}$$

The form of A_{Pn} is similar to the weak-anisotropy approximation for the normal-moveout velocity in a horizontal VTI layer (Thomsen 1986; Tsvankin 2012).

Replacing the attenuation-anisotropy parameters ε_Q and δ_Q by A_{Ph} and A_{Pn} is convenient for inversion purposes because A_{P0}, A_{S0}, A_{Ph} and A_{Pn} have the same units and similar magnitudes. The gradients for the attenuation parameters can be obtained from those for the stiffness differences ΔC_{ijkl} by applying the chain rule (Bai *et al.* 2017). The limited-memory Broyden-Fletcher-Goldfarb-Shanno (L-BFGS) method (Nocedal 1980) is used in parameter updating to scale the gradients by an approximate inverse Hessian matrix.

2.3 Source-independent viscoelastic waveform inversion

In the time domain, the displacement can be expressed as the convolution of the Green's function and the source wavelet (Choi and Alkhalifah 2011). Then equation (5) can be represented as

$$F(\mathbf{m}) = \frac{1}{2} \parallel \mathbf{G_u} * \mathbf{s_u} - \mathbf{G_d} * \mathbf{s_d} \parallel^2, \tag{9}$$

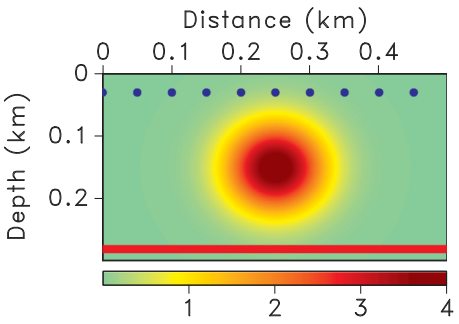

Figure 1 Gaussian anomaly in the parameter A_{S0} embedded in a homogeneous VTI medium. The plot shows the fractional difference between A_{S0} and its background value, 0.005 ($Q_{S0} \approx 100$); at the centre of the anomaly, $A_{S0} = 0.025$ ($Q_{S0} \approx 20$). The other medium parameters are constant: $A_{P0} = 0.005$, $\varepsilon_Q = -0.2$, $\delta_Q = -0.4$, $V_{P0} = 4000$ m/s, $V_{S0} = 2000$ m/s, $\varepsilon = 0.15$, $\delta = 0.1$ and $\rho = 2000\,\mathrm{kg/m^3}$. The model size is 500 m × 300 m, with grid spacing $\Delta x = \Delta z = 1$ m. The blue dots denote the horizontal-displacement sources, and the magenta line marks the receivers placed at each grid point at the bottom of the model.

where $*$ is the convolution operator, $\mathbf{G}$ denotes the Green's function, $\mathbf{s}$ is the source wavelet and the subscripts $\mathbf{u}$ and $\mathbf{d}$ refer to the simulated and observed wavefields, respectively. Because the source signature is difficult to estimate in practice (i.e. $\mathbf{s_u} \neq \mathbf{s_d}$), the conventional objective function (equation (5)) introduces distortions in the inverted model parameters represented by $\mathbf{G_u}$ (see examples below).

To address this problem, Choi and Alkhalifah (2011) introduce a 'source-independent' objective function, which has the following form:

$$F = \frac{1}{2} \parallel \mathbf{u} * \mathbf{d}^{\mathrm{ref}} - \mathbf{d} * \mathbf{u}^{\mathrm{ref}} \parallel^2, \tag{10}$$

or

$$F = \frac{1}{2} \parallel (\mathbf{G_u} * \mathbf{s_u}) * (\mathbf{s_d} * \mathbf{G_d^{ref}}) - (\mathbf{G_d} * \mathbf{s_d}) * (\mathbf{s_u} * \mathbf{G_u^{ref}}) \parallel^2, \tag{11}$$

where the superscript 'ref' denotes reference traces from the simulated and observed data. The new objective function is designed to remove the influence of the source signature on parameter updating. The first-order data residual, which acts as the adjoint source, is derived by Choi and Alkhalifah (2011; see Appendix A):

$$\mathbf{r} = \mathbf{d}^{\mathrm{ref}} \otimes \left(\mathbf{u} * \mathbf{d}^{\mathrm{ref}} - \mathbf{d} * \mathbf{u}^{\mathrm{ref}} \right), \tag{12}$$

where $\otimes$ denotes cross-correlation.

3 SYNTHETIC EXAMPLES

3.1 Transmission tests

Here, we conduct a transmission experiment to evaluate the crosstalk between the source signature and the model (i.e. attenuation) parameters and to demonstrate that the source-independent algorithm can mitigate this crosstalk for anisotropic media.

A Gaussian anomaly in the shear-wave attenuation parameter A_{S0} is inserted between displacement sources and receivers embedded in a homogeneous VTI medium (Fig. 1). The other three Thomsen-style attenuation parameters (A_{P0}, ε_Q and δ_Q) are constant. The four VTI velocity parameters (V_{P0}, V_{S0}, ε and δ) and density are also constant and kept at their actual values during the inversion.

The source signal used to generate the observed data represents the first derivative of the Ricker wavelet (Fig. 2a). The reference frequency, which determines the peak attenuation, is equal to the central frequency of the wavelet (30 Hz). The homogeneous VTI background is chosen as the initial model; the attenuation parameters A_{P0}, A_{S0}, A_{Ph} and A_{Pn} are updated simultaneously.

Figure 3 shows the inversion result obtained with the actual wavelet. Similar to the results of the transmission experiment in Bai *et al.* (2017), the conventional waveform inversion (WI) algorithm is able to reconstruct most of the anomaly in A_{S0}. The peak of the estimated anomaly is $A_{S0} = 0.021$ (or $Q_{S0} = 23.8$), whereas the actual value

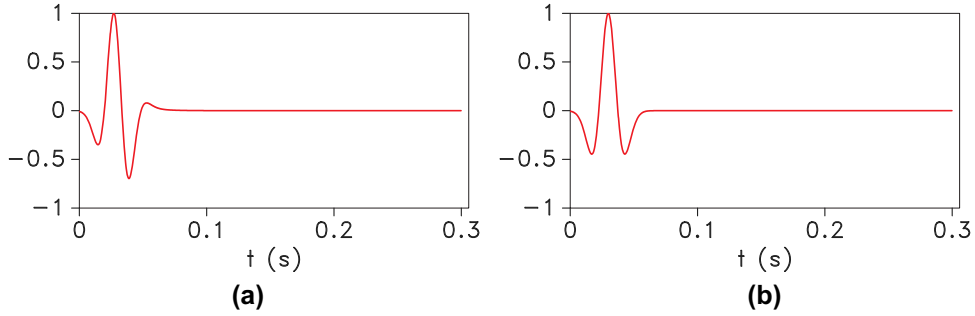

Figure 2 (a) Source wavelet used to generate the 'observed' data. (b) The trial wavelet used to obtain the inversion results in Figures 5 and 6.

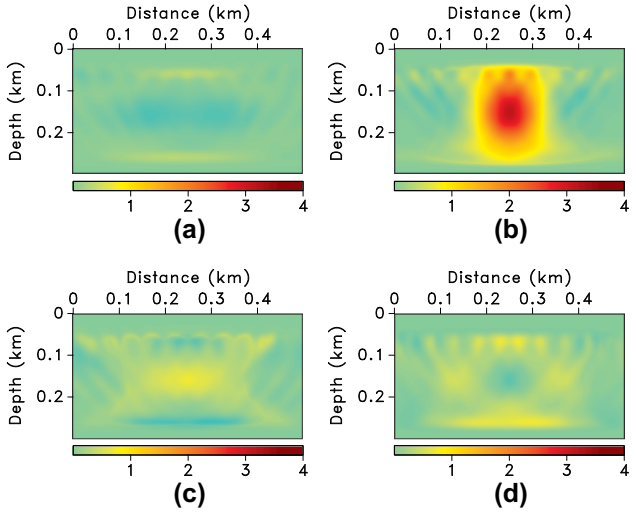

Figure 3 Fractional differences between the inverted and initial parameters for the model from Figure 1: (a) A_{P0}, (b) A_{S0}, (c) A_{Pb} and (d) A_{Pn}. Waveform inversion is conducted with the actual wavelet (Fig. 2a) using the conventional ℓ_2-norm objective function in equation (5). The peak value of the recovered anomaly in A_{S0} is 0.021 (about 84% of the actual maximum).

is 0.025 (or $Q_{S0} = 20$). The parameters A_{P0}, A_{Pb} and A_{Pn} are practically unchanged, which indicates the absence of crosstalk between A_{S0} and other attenuation parameters in this (favourable) acquisition geometry. The objective function using the actual wavelet rapidly decreases to less than 1% of the original value (Fig. 4, red curve).

However, in practice the source signature is seldom known and has to be estimated from the data. To test the sensitivity of the viscoelastic waveform inversion to the source signature, we replace the actual signal in Figure 2(a) with a

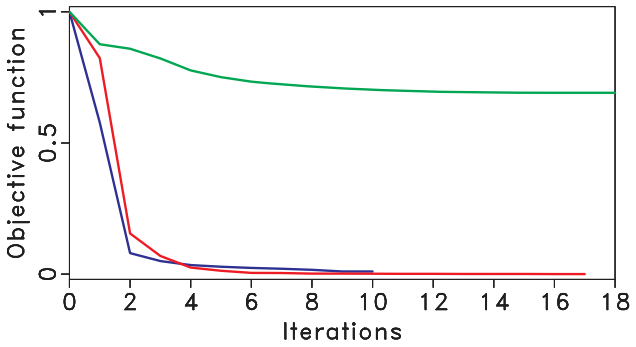

Figure 4 Normalized objective functions for the transmission tests. The conventional WI with the actual wavelet (Fig. 3, red curve); the conventional WI with the trial wavelet (Fig. 5, green curve); and the SIWI with the trial wavelet (Fig. 6, blue curve).

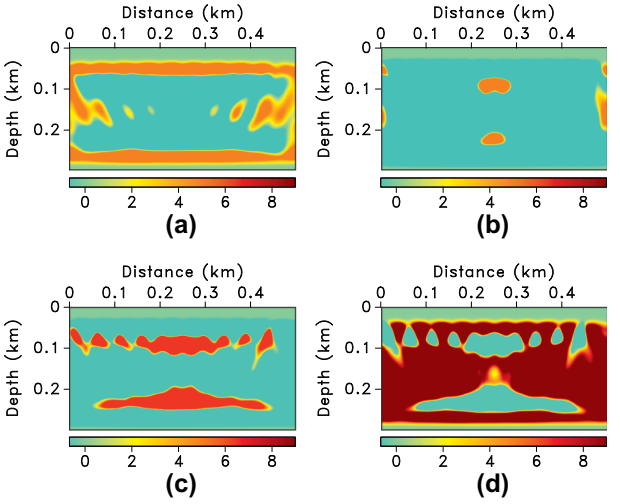

Figure 5 Inversion results obtained by conventional WI with the trial wavelet from Figure 2(b). The inverted parameters (a) A_{P0}, (b) A_{S0}, (c) A_{Pb} and (d) A_{Pn}.

Ricker wavelet that has a central frequency of 30 Hz (Fig. 2b). The inverted attenuation parameters are strongly distorted; the anomaly in A_{S0} is completely smeared, and there is a significant leakage from A_{S0} into the other parameters (Fig. 5). In some parts of the model, the inverted parameters reach their lower and upper limits set in the algorithm. These results confirm the strong crosstalk between the source signature and attenuation parameters. The distorted source wavelet prevents the conventional WI algorithm from converging towards the actual model (Fig. 4).

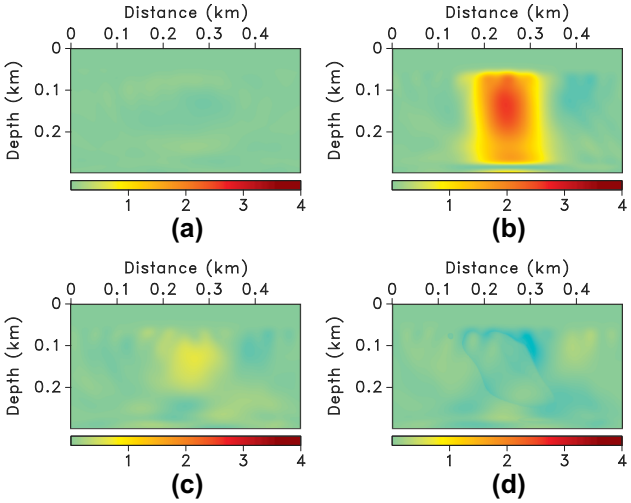

Figure 6 Inversion results obtained by the proposed source-independent algorithm with the trial wavelet from Figure 2(b). The inverted parameters (a) A_{P0}, (b) A_{S0}, (c) A_{Pb} and (d) A_{Pn}.

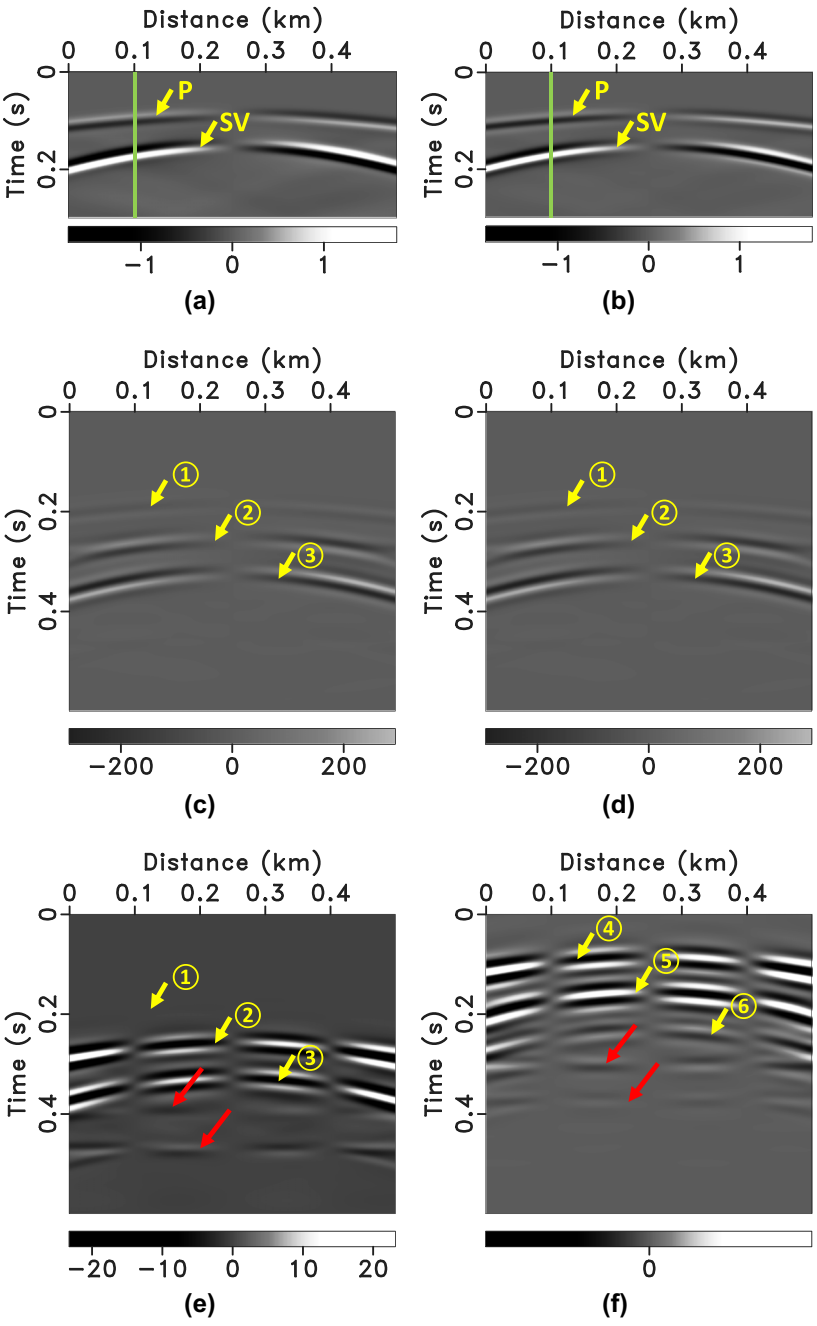

Figure 7 (a) Simulated (at first iteration) and (b) observed vertical displacement for the test in Figure 6; the source is located at $x = 0.25$ km. The convolved data sets (c) $\mathbf{u} * \mathbf{d}^{\text{ref}}$ and (d) $\mathbf{d} * \mathbf{u}^{\text{ref}}$. (e) The difference $(\mathbf{u} * \mathbf{d}^{\text{ref}} - \mathbf{d} * \mathbf{u}^{\text{ref}})$ between (c) and (d). (f) The first-order residual $\mathbf{d}^{\text{ref}} \otimes (\mathbf{u} * \mathbf{d}^{\text{ref}} - \mathbf{d} * \mathbf{u}^{\text{ref}})$. The green lines on plots (a) and (b) denote the reference traces, and the red arrows in (e) and (f) point to induced artefacts. The marked events are (1) P∗P, (2) P∗S (also includes S∗P), (3) S∗S, (4) P⊗(P∗P)+S⊗(P∗S), (5) S⊗(S∗S)+P⊗(P∗S) and (6) P⊗(S∗S).

Next, we apply the proposed source-independent waveform inversion (SIWI) algorithm with the reference traces from the observed and simulated data recorded at $x = 0.1$ km. After 10 iterations, the algorithm reconstructs most of the A_{S0} anomaly, and there is almost no crosstalk with the other attenuation parameters (Fig. 6). However, the coefficient A_{S0} is estimated with less accuracy (Fig. 6b) compared to the WI result obtained with the actual wavelet (Fig. 3b). The peak of the A_{S0} anomaly is substantially underestimated, and the anomaly's shape is distorted. This deterioration in the inversion results is due to the increased nonlinearity of the inverse problem caused by the cross-correlation and convolution operations in the SIWI algorithm (Choi and Alkhalifah 2011).

Figure 7 illustrates the generation of the first-order data residual (or the adjoint source) in the first iteration of model updating with the SIWI. Using the simulated (Fig. 7a) and

observed (Fig. 7b) data and the reference traces at $x = 0.1$ km (green line), we compute the convolved data sets $\mathbf{u} * \mathbf{d}^{\text{ref}}$ (Fig. 7c) and $\mathbf{d} * \mathbf{u}^{\text{ref}}$ (Fig. 7d). After the convolution, we observe three events: (1) P∗P, (2) P∗S+S∗P and (3) S∗S. Figure 7(e) displays the difference between the two convolved data sets (i.e. $\mathbf{u} * \mathbf{d}^{\text{ref}} - \mathbf{d} * \mathbf{u}^{\text{ref}}$). Our choice of the reference trace (green line) results in blank records at $x = 0.1$ km and $x = 0.4$ km (due to the symmetry).

Because the anomaly is introduced only in the parameter A_{S0}, which has almost no influence on P-waves, there should be no data residual for events involving just P-modes. This explains the elimination of the event corresponding to the P-P convolution after the subtraction (event 1 in Fig. 7e). The oscillations at times close to 0.3 s in the simulated and observed data produce artefacts in Figure 7(c) and 7(d) that are also visible in the difference between the convolved data sets (see the red arrows in Fig. 7e). Finally, Figure 7(f) shows the first-order data residuals [i.e. $\mathbf{d}^{\text{ref}} \otimes (\mathbf{u} * \mathbf{d}^{\text{ref}} - \mathbf{d} * \mathbf{u}^{\text{ref}})$], in which time shifts caused by the convolution operations are corrected by the cross-correlation. Reducing the time window to the original data size (0.3 s) allowed us to suppress most artefacts.

Figure 8 shows the initial and final data residuals for the conventional WI applied with the actual wavelet (Fig. 8a,b) and for the proposed SIWI method with the trial wavelet (Fig. 8c,d). The data residuals (or the adjoint sources) for SIWI have a more complex structure (compare Fig. 8c with Fig. 8a), but both inversion methods provide a comparable improvement in data-fitting (this is also reflected in the objective functions in Fig. 4).

The source-independent objective function (equation (11)) can be viewed as the conventional function (equation (9)) applied with a low-pass-filtered source $\mathbf{s}_u * \mathbf{s}_d$. Hence, for transmission tests with anomalies in the parameters A_{P0} and ε_Q, we expect the SIWI results to be slightly inferior to those in Bai *et al.* (2017).

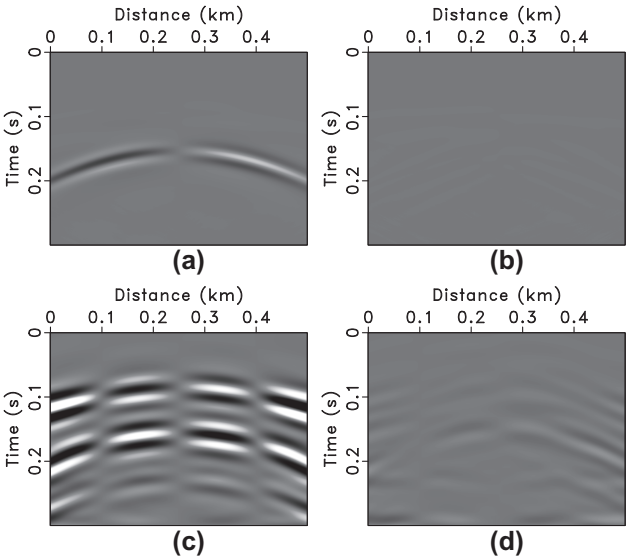

Figure 8 Data residuals before [(a) and (c)] and after [(b) and (d)] the inversion. Gathers (a) and (b) are generated by the conventional WI with the actual wavelet, whereas (c) and (d) by the SIWI algorithm with the trial wavelet. Plots (a) and (b) are on the same scale; plots (c) and (d) also are on the same scale.

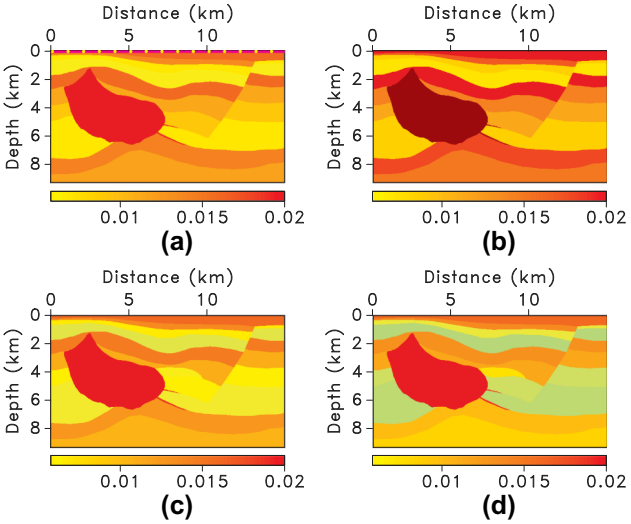

Figure 9 Attenuation parameters for the modified Hess VTI model: (a) A_{P0}, (b) A_{S0}, (c) A_{Pb} and (d) A_{Pn}. The model size is 15,000 m × 9375 m, with grid spacing $\Delta x = \Delta z = 25$ m. The yellow dots on plot (a) denote displacement sources, and the magenta line marks the receivers.

3.2 Test for surface data

Next, we test the performance of the SIWI algorithm on reflection data generated for the modified Hess VTI model (fashioned after sections from the Gulf of Mexico), which includes anisotropic attenuation (Fig. 9). The velocity parameters and density (not shown here) have a structure similar to that of the attenuation parameters (Han *et al.* 2001; Tsvankin 2012). The model is strongly heterogeneous with such complex features as folding, a fault and a salt body. The wavefield is generated by 15 oblique displacement sources evenly spaced at a depth of 75 m, which excite a wavelet with a central frequency of 40 Hz (the first derivative of the Ricker wavelet, Fig. 10a). The initial attenuation parameters (Fig. 11) are obtained by applying triangle filtering to the actual parameter fields with a smoothing radius of 20 samples in the vertical and horizontal

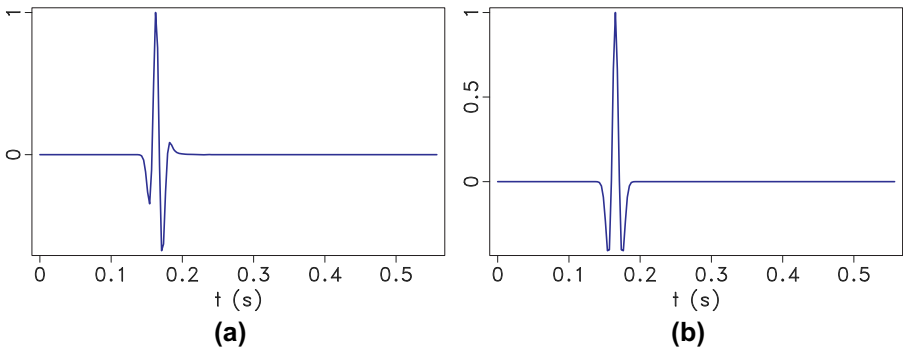

Figure 10 (a) Actual and (b) trial source wavelet used for the model in Figure 9. The central frequency is approximately 40 Hz.

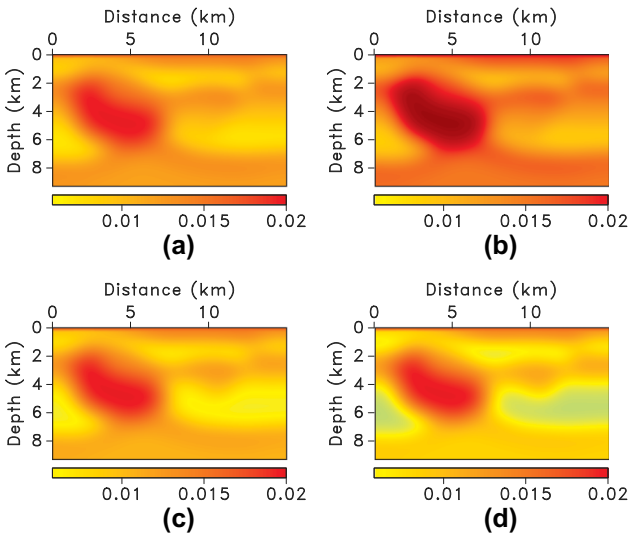

Figure 11 Initial attenuation parameters for the model in Figure 9: (a) A_{P0}, (b) A_{S0}, (c) A_{Ph} and (d) A_{Pn}. The initial model is obtained by smoothing the actual parameters with triangle filtering that has a smoothing radius of 20 samples in both the vertical and horizontal directions.

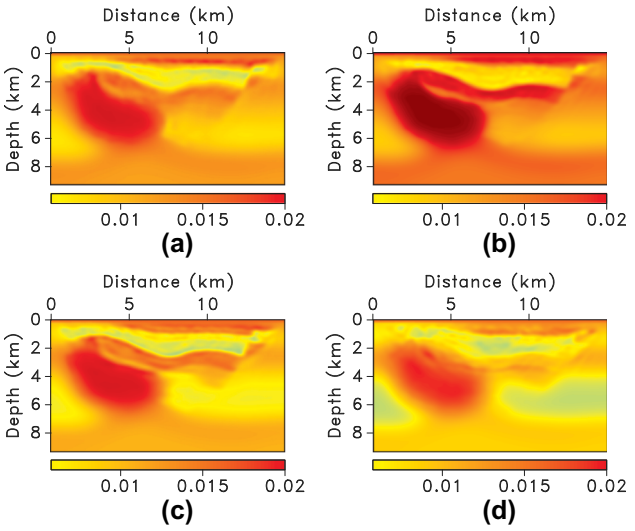

Figure 12 Inverted attenuation parameters (a) A_{P0}, (b) A_{S0}, (c) A_{Ph} and (d) A_{Pn} obtained by the conventional WI with the actual wavelet (Figure 10a).

directions. In practice, a smooth attenuation model can be obtained by applying the spectral ratio method for anisotropic media combined with layer stripping (Behura and Tsvankin 2009).

First, we mute the direct arrivals and perform conventional WI with the actual wavelet (Fig. 10a). After 18 iterations, the algorithm produces sufficiently accurate estimates of the attenuation parameters, especially A_{P0}, A_{S0} and A_{Ph} (Fig. 12). The boundaries of the salt body, the folded layers (in particular, the one at depths between 2 and 4 km) and the fault surface (at a horizontal distance of around 13 km and depth of 2 km) are well delineated. The vertical parameter profiles (Fig. 13) illustrate the convergence towards the actual values down to the depth of 4 km; the evolution of the objective function is shown in Figure 18.

Next, conventional WI is applied with a trial wavelet (Fig. 10b). The wavelet distortion prevents the algorithm from updating the attenuation parameters for this model. To implement the proposed SIWI methodology, we choose the truncated near-offset (25 m) seismograms containing the direct P-arrival (Fig. 14) as the reference traces. SIWI helps recover the long-wavelength model features in the shallow part of the section (Fig. 15). Yet, the folded layers at depths between 2 and 4 km are mispositioned and the fault is somewhat smeared. These problems, along with the behaviour of the objective function (the red curve in Fig. 18), indicate that the SIWI model-updating process get trapped in local minima caused by the increased nonlinearity of the inverse problem.

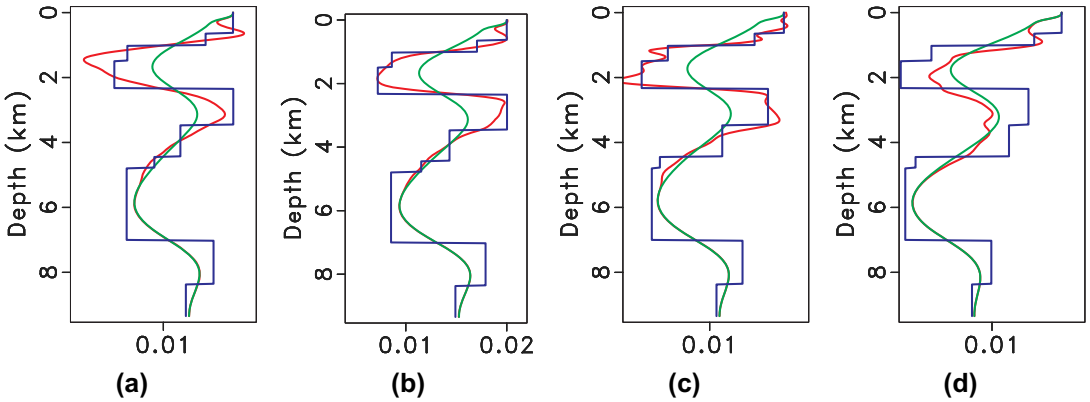

Figure 13 Profiles of the attenuation parameters at $x = 11.25$ km: (a) A_{P0}, (b) A_{S0}, (c) A_{Pb} and (d) A_{Pn}. The red lines are the parameters estimated by the conventional WI with the actual wavelet (Fig. 12). The blue and green lines mark the actual and initial parameters, respectively.

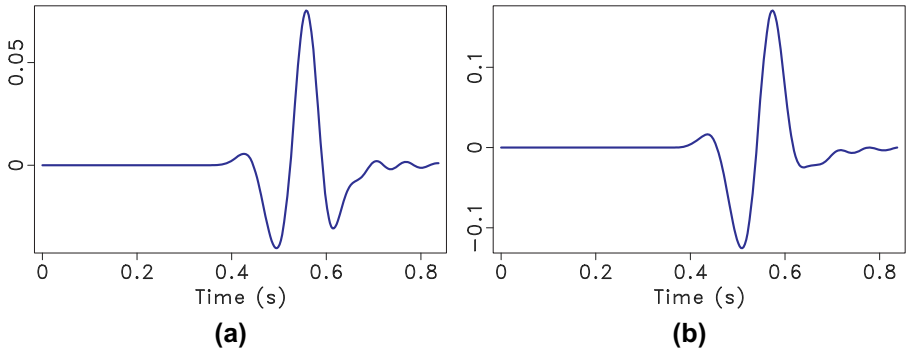

Figure 14 Reference traces (at $x = 7.025$ km) for the source at $x = 7$ km, which were extracted from the (a) observed and (b) simulated data.

Therefore, we repeat the SIWI experiment using improved initial parameter fields (Fig. 16). This initial model helps obtain more accurate attenuation parameters (Fig. 17), which provide better data fitting (see the corresponding objective function in Fig. 18).

3.3 Mitigation of velocity errors

In addition to the unknown source signature, the results of attenuation estimation can be also hampered by inaccurate velocity fields. In our previous publication (Bai *et al.* 2017), we employed a local-similarity method (Fomel 2009) to suppress the influence of velocity errors on modelled travel times. To evaluate the impact of velocity distortions on the inverted attenuation parameters, we reproduce the test in Figure 17 with the vertical P- and S-wave velocities (V_{P0} and V_{S0}) reduced throughout the section to 95% of the actual values. The 5% velocity error turns out to be sufficient to cause a breakdown of the proposed SIWI algorithm (these results are not shown here). Therefore, following Bai *et al.* (2017), we calculate the time shifts between the two convolved data sets ($\mathbf{u} * \mathbf{d}^{\text{ref}}$ and $\mathbf{d} * \mathbf{u}^{\text{ref}}$) with an estimated local-similarity map (Fomel 2009). The SIWI objective function (equation (10)) can be modified as

$$F = \frac{1}{2} \parallel [\mathbf{u}(t, \mathbf{m}) * \mathbf{d}^{\text{ref}}(t)] - \mathbf{S}(t)\, [\mathbf{d}(t) * \mathbf{u}^{\text{ref}}(t, \mathbf{m})] \parallel^2, \qquad (13)$$

where $\mathbf{S}(t)$ is the time-shift operator calculated from the local-similarity map.

The first-order data residual then becomes

$$\mathbf{r} = \mathbf{d}^{\text{ref}} \otimes \left[\left(\mathbf{u} * \mathbf{d}^{\text{ref}} \right) - \mathbf{S} \left(\mathbf{d} * \mathbf{u}^{\text{ref}} \right) \right]. \qquad (14)$$

After the local-similarity-based correction, the algorithm generates more accurate adjoint sources (compare Fig. 19e with Fig. 19d). The objective function after SIWI is reduced by about 75%, but velocity-related amplitude distortions leak into the inverted attenuation parameters. The inversion errors are especially visible in the folded layers at depths between 1 and 3 km in Figure 20 (compare with Fig. 17). Clearly, despite the improvements provided by the local-similarity technique, sufficiently accurate velocity fields are required for robust attenuation estimation.

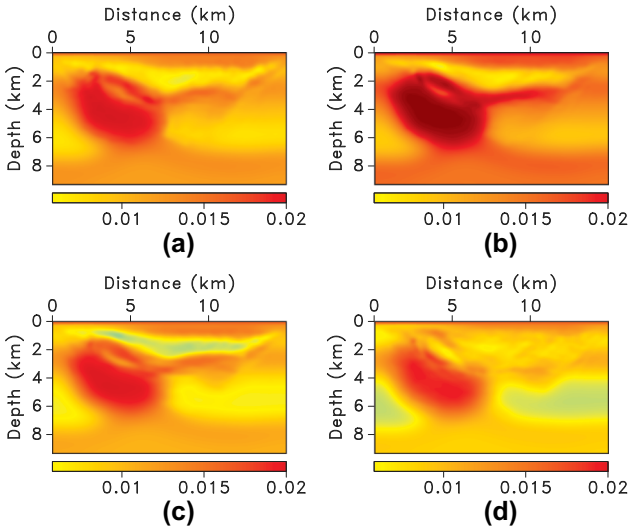

Figure 15 Inverted attenuation parameters (a) A_{P0}, (b) A_{S0}, (c) A_{Ph} and (d) A_{Pn} obtained by the proposed SIWI algorithm with the trial wavelet (Fig. 10b).

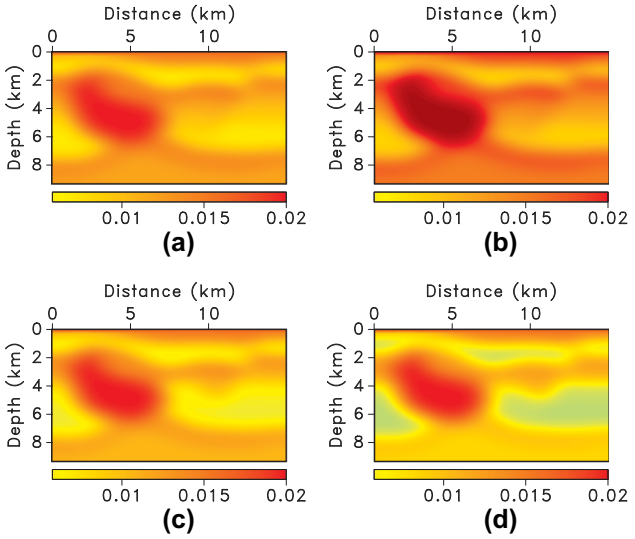

Figure 16 Initial attenuation parameters (a) A_{P0}, (b) A_{S0}, (c) A_{Ph} and (d) A_{Pn} obtained by smoothing with a triangle filtering that has a smoothing radius of 15 samples in the vertical direction and 20 samples in the horizontal direction. This initial model is more accurate than the one in Figure 11.

4 DISCUSSION

Because attenuation estimation is performed with the actual velocity model in most experiments here (section 3.1–3.2), the Green's functions in equation (11) are dominantly influenced by the attenuation parameters. However, the reference frequency, at which the peak attenuation is

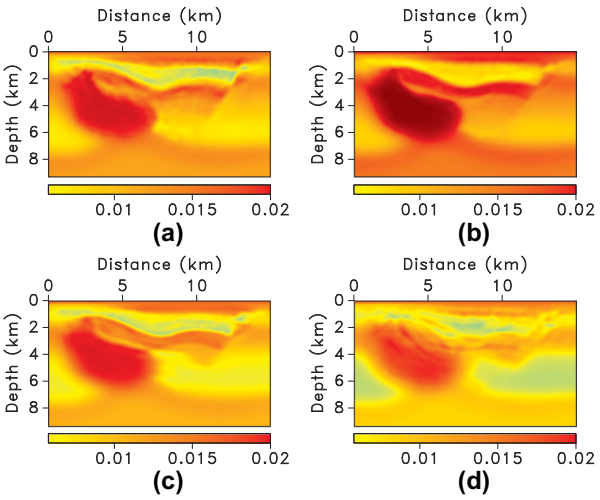

Figure 17 Inverted attenuation parameters (a) A_{P0}, (b) A_{S0}, (c) A_{Ph} and (d) A_{Pn} obtained by the proposed SIWI algorithm with the trial wavelet using the initial model in Figure 16.

generated in time-domain simulations with one relaxation mechanism, also contributes to the Green's function. Here, we facilitate the inversion by choosing the same reference frequency for simulating the 'observed' and modelled data. As a result, the objective function in equation (11) is minimized for the actual attenuation parameters (i.e. for $\mathbf{G_u} = \mathbf{G_d}$). However, the inversion may become problematic if the reference frequency for the trial simulation significantly differs from that for the observed data (i.e. if $f^u_{\text{ref}} \neq f^d_{\text{ref}}$). In that

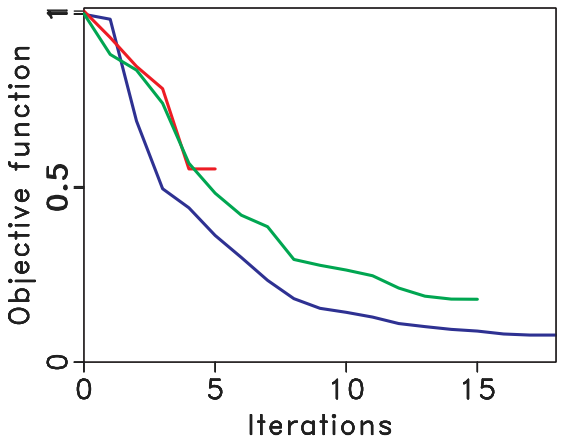

Figure 18 Normalized objective function for the reflection experiments (see the model in Fig. 9). The conventional WI with the actual wavelet (Fig. 12, blue curve); the SIWI with the trial wavelet using the initial model in Figure 11 (Fig. 15, red curve), which stopped after six iterations; and the SIWI with the trial wavelet using a better initial model (Fig. 17, green curve).

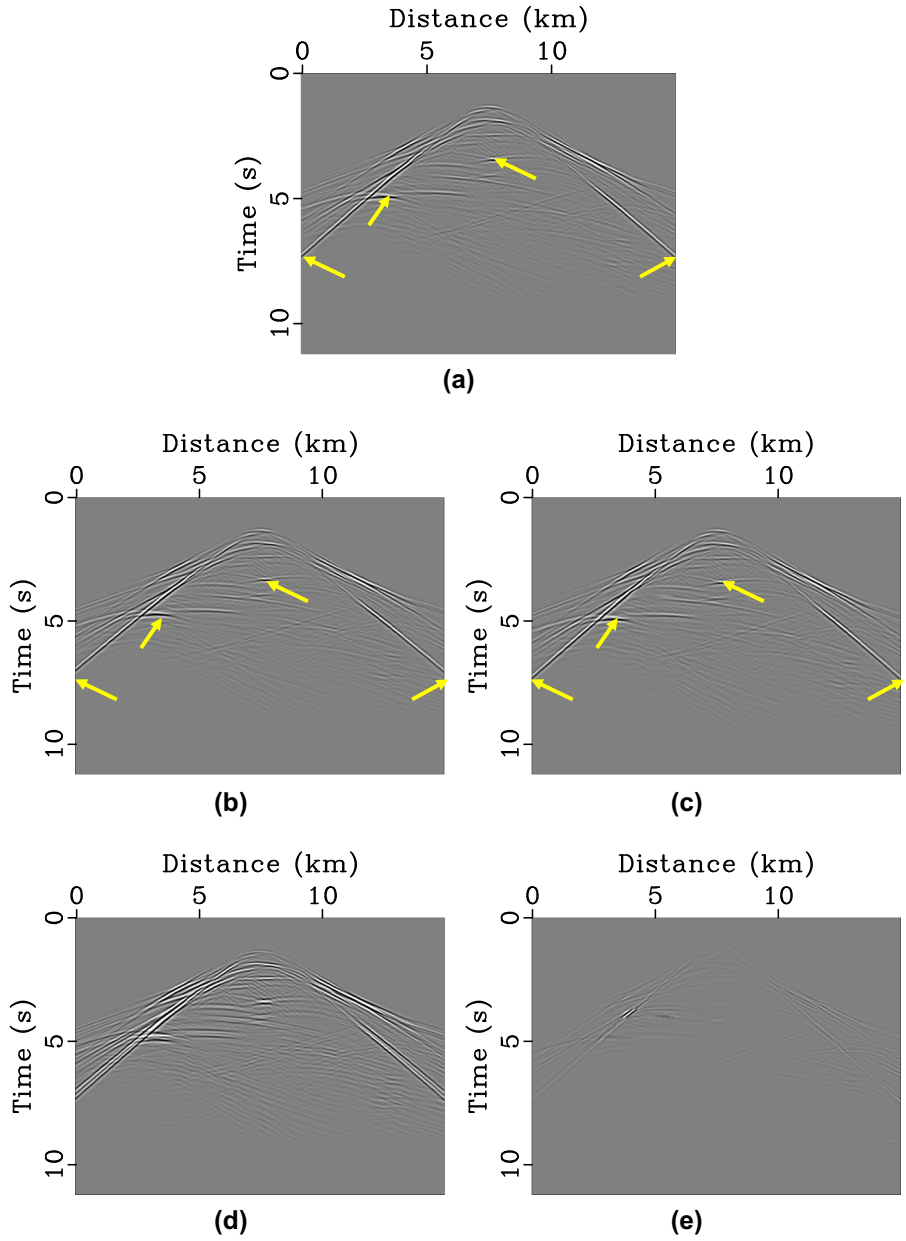

Figure 19 Convolved data sets (horizontal displacement at first iteration): (a) $\mathbf{u} * \mathbf{d}^{\text{ref}}$ and (b) $\mathbf{d} * \mathbf{u}^{\text{ref}}$ for the test with velocities V_{P0} and V_{S0} distorted by 5%; the source is located at $x = 8$ km. (c) The convolved data $\mathbf{d} * \mathbf{u}^{\text{ref}}$ from plot (b) after applying the local-similarity technique. (d) The difference between (a) and (b); and (e) the difference between (a) and (c). All gathers are on the same scale. The yellow arrows show events from the data set $\mathbf{d} * \mathbf{u}^{\text{ref}}$ that have been aligned with the corresponding ones from $\mathbf{u} * \mathbf{d}^{\text{ref}}$ after application of local similarity.

case, when the waveform-inversion algorithm tries to find the desired value A_1 at f^d_{ref} (Fig. 21), it will instead obtain a different value A_2 from the attenuation curve for the assumed reference frequency f^u_{ref}. For instance, we repeated the transmission experiment in Fig. 1 with $f^u_{\text{ref}} = 100$ Hz (whereas $f^d_{\text{ref}} = 30$) and obtained substantially distorted inversion results (not shown here).

The influence of the reference frequency can be mitigated by simulating less varying or even constant quality-factor elements Q_{ij} over the entire frequency band of the seismic data. However, this requires the inclusion of several relaxation mechanisms and, consequently, several additional coefficients corresponding to the characteristic (reference) frequencies. To avoid estimating these extra parameters, it may be possible to

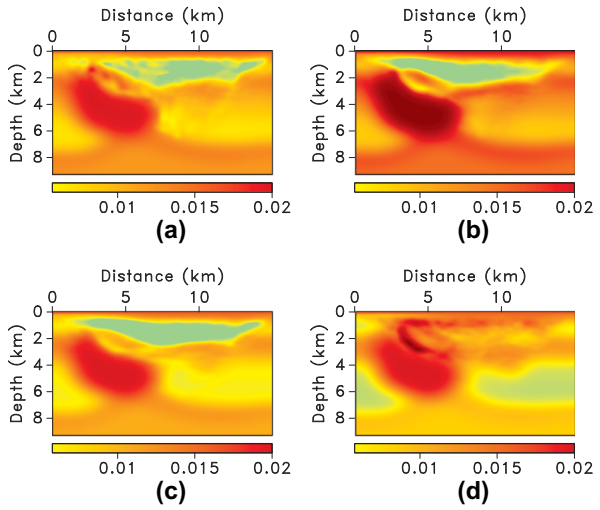

Figure 20 Inverted attenuation parameters (a) A_{P0}, (b) A_{S0}, (c) A_{Ph} and (d) A_{Pn} obtained by SIWI. The algorithm is applied with the trial wavelet using the initial attenuation model in Figure 16 and distorted velocities (V_{P0} and V_{S0} are reduced by 5% from the actual values). The influence of the velocity errors is mitigated by applying the local-similarity technique (see Fig. 19).

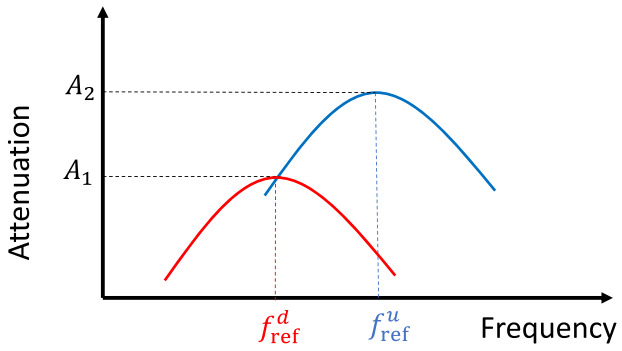

Figure 21 Schematic diagram showing the influence of the reference frequency on WI-based attenuation estimation. The two curves have different peak magnitudes (A_1 and A_2) at their reference frequencies (f^d_{ref} and f^u_{ref}) but generate the attenuation coefficient with the same magnitude at frequency f^d_{ref}.

employ a set of fixed coefficients for typical Q-values in the subsurface (e.g. to use the same set of coefficients to simulate $Q = 20$ and $Q = 500$; see Fichtner and Van Driel 2014).

For purposes of quantitative reservoir characterization, macroscale seismic attributes could be linked to microscale rock physics properties through the effective poroelastic parameters (e.g. Dupuy *et al.* 2016). Whereas the constant-Q assumption is widely adopted in seismic processing and inversion, it becomes inadequate for a wider frequency range also covering sonic and core measurements. A better understanding of the frequency-dependent Q-behaviour could help in filling the data gaps between different frequency bands. For example, ultrasonic laboratory measurements of attenuation can potentially provide useful constraints for seismic attenuation analysis. Also, mesoscale Q-values, which could be related to permeability and other critically important reservoir properties, might be inferred from either microscale (rock physics) or macroscale (seismic) measurements (e.g. Ali and Jakobsen 2011).

5 CONCLUSIONS

We extended the source-independent waveform inversion (SIWI) methodology to attenuation estimation in heterogeneous transversely isotropic media with a vertical symmetry axis. The SIWI objective function, designed to suppress the influence of errors in the source wavelet, is defined as the ℓ_2-norm of the difference between two additionally generated data sets. The approximate adjoint source is obtained as the zero-lag cross-correlation of the reference trace from the observed data with that data difference. The gradients for the attenuation parameters are computed with the adjoint-state method in the same way as in our previously developed waveform inversion (WI) algorithm.

First, we examined the influence of the source signature on attenuation estimation using transmission data from a homogeneous background VTI model with a Gaussian anomaly in the shear-wave attenuation parameter A_{S0}. Whereas conventional WI with the actual wavelet produces satisfactory inversion results, a slight (mainly phase) distortion of the wavelet results in erroneous attenuation parameters. In contrast, the proposed SIWI algorithm generates satisfactory inversion results (albeit with a somewhat lower resolution) despite the wavelet distortion.

The algorithm was also tested on synthetic reflection data from a modified Hess VTI model, which contains a fault, a salt body and folding layers. Muting the direct arrivals and conducting WI with the actual wavelet yields a sufficiently accurate long- and intermediate-wavelength attenuation model with well-delineated structural boundaries. However, when a distorted trial wavelet is used, the conventional algorithm completely fails to update the initial model. The proposed SIWI with the trial wavelet employed the windowed direct P-arrivals as the reference traces. The algorithm successfully reconstructed long-wavelength features of the attenuation model, although some short-wavelength components could not be resolved (e.g. the folded layers were mispositioned) due to the increased nonlinearity of the inverse problem. A better initial model made it possible for SIWI to avoid local

minima of the objective function and obtain more accurate attenuation parameters. We also showed that the influence of errors in VTI velocity parameters can be reduced by incorporating the local-similarity method.

ACKNOWLEDGEMENTS

This work was supported by the Consortium Project on Seismic Inverse Methods for Complex Structures at the Center for Wave Phenomena, Colorado School of Mines. The reproducible numeric examples in this paper are generated with the Madagascar open-source software package freely available from http://www.ahay.org.

REFERENCES

Ali A. and Jakobsen M. 2011. Seismic characterization of reservoirs with multiple fracture sets using velocity and attenuation anisotropy data. *Journal of Applied Geophysics* **75**, 590–602.

Bai J. and Yingst D. 2013. Q estimation through waveform inversion. 75th EAGE Conference & Exhibition.

Bai T. and Tsvankin I. 2016. Time-domain finite-difference modeling for attenuative anisotropic media. *Geophysics* **81**, C69–C77.

Bai T., Tsvankin I. and Wu X. 2017. Waveform inversion for attenuation estimation in anisotropic media. *Geophysics* **82**, WA83–WA93.

Bai T., Zhu T. and Tsvankin I. 2019. Attenuation compensation for time-reversal imaging in VTI media. *Geophysics* **84**, 1–99.

Behura J. and Tsvankin I. 2009. Estimation of interval anisotropic attenuation from reflection data. *Geophysics* **74**, no. 6, A69–A74.

Best A.I., Sothcott J. and McCann C. 2007. A laboratory study of seismic velocity and attenuation anisotropy in near-surface sedimentary rocks. *Geophysical Prospecting* **55**, 609–625.

Carcione J.M., Morency C. and Santos J.E. 2010. Computational poroelasticity—a review. *Geophysics* **75**, 75A229–75A243.

Causse E., Mittet R. and Ursin B. 1999. Preconditioning of full-waveform inversion in viscoacoustic media. *Geophysics* **64**, 130–145.

Charara M., Barnes C. and Tarantola A. 2000. Full waveform inversion of seismic data for a viscoelastic medium. In *Methods and Applications of Inversion* (eds. Per C. Hansen, B.H. Jacobsen and K. Mosegaard), pp. 68–81. Springer.

Choi Y. and Alkhalifah T. 2011. Source-independent time-domain waveform inversion using convolved wavefields: application to the encoded multisource waveform inversion. *Geophysics* **76**, R125–R134.

de Castro Nunes B.I., De Medeiros W.E., do Nascimento A.F. and de Morais Moreira J.A. 2011. Estimating quality factor from surface seismic data: a comparison of current approaches. *Journal of Applied Geophysics* **75**, 161–170.

Donald J., Butt S. and Iakovlev S. 2004. Adaptation of a triaxial cell for ultrasonic P-wave attenuation, velocity and acoustic emission measurements. *International Journal of Rock Mechanics and Mining Sciences* **41**, 1001–1011.

Dupuy B., Asnaashari A., Brossier R., Garambois S., Métivier L., Ribodetti A. and Virieux J. 2016. A downscaling strategy from FWI to microscale reservoir properties from high-resolution images. *The Leading Edge* **35**, 146–150.

Ekanem A., Wei J., Li X.-Y., Chapman M. and Main I. 2013. P-wave attenuation anisotropy in fractured media: a seismic physical modelling study. *Geophysical Prospecting* **61**, 420–433.

Fichtner A. 2005. The adjoint method in seismology: theory and application to waveform inversion. AGU Fall Meeting Abstracts, 06.

Fichtner A. and Van Driel M. 2014. Models and Fréchet kernels for frequency-(in) dependent *Q*. *Geophysical Journal International* **198**, 1878–1889.

Fomel S. 2009. Velocity analysis using AB semblance. *Geophysical Prospecting* **57**, 311–321.

Groos L., Schäfer M., Forbriger T. and Bohlen T. 2014. The role of attenuation in 2D full-waveform inversion of shallow-seismic body and Rayleigh waves. *Geophysics* **79**, R247–R261.

Guo P. and McMechan G.A. 2017. Sensitivity of 3D 3C synthetic seismograms to anisotropic attenuation and velocity in reservoir models. *Geophysics* **82**, no. 2, T79–T95.

Han B., Galikeev T., Grechka V., Rousseau J. and Tsvankin I. 2001. A synthetic example of anisotropic P-wave processing for a model from the Gulf of Mexico. *Anisotropy 2000: Fractures, Converted Waves, and Case Studies* (eds. L. Ikelle and A. Gangi), pp. 311–325. Society of Exploration Geophysicists.

Kamei R. and Pratt R.G. 2008. Waveform tomography strategies for imaging attenuation structure with cross-hole data. 70th EAGE Conference & Exhibition, F019.

Krzikalla F. and Müller T.M. 2011. Anisotropic P-SV-wave dispersion and attenuation due to inter-layer flow in thinly layered porous rocks. *Geophysics* **76**, WA135–WA145.

Kurzmann A., Przebindowska A., Köhn D. and Bohlen T. 2013. Acoustic full waveform tomography in the presence of attenuation: a sensitivity analysis. *Geophysical Journal International* **195**, 985–1000.

Luo C., Yuan S. and Wang S. 2014. Influence of inaccurate wavelet phase estimation on prestack waveform inversion, SEG Technical Program Expanded Abstracts 2014, 3247–3251.

Müller T.M., Gurevich B. and Lebedev M. 2010. Seismic wave attenuation and dispersion resulting from wave-induced flow in porous rocks—a review. *Geophysics* **75**, 75A147–75A164.

Nocedal J. 1980. Updating quasi-Newton matrices with limited storage. *Mathematics of Computation* **35**, 773–782.

Plessix R., Milcik P., Rynja H., Stopin A., Matson K. and Abri S. 2013. Multiparameter full-waveform inversion: marine and land examples. *The Leading Edge* **32**, 1030–1038.

Prieux V., Brossier R., Operto S. and Virieux J. 2013. Multiparameter full waveform inversion of multicomponent ocean-bottom-cable data from the valhall field. Part 1: imaging compressional wave speed, density and attenuation. *Geophysical Journal International* **194**, 1640–1664.

Quan Y. and Harris J.M. 1997. Seismic attenuation tomography using the frequency shift method. *Geophysics* **62**, 895–905.

Rao Y. and Wang Y. 2009. Fracture effects in seismic attenuation images reconstructed by waveform tomography. *Geophysics* **74**, R25–R34.

Sams M. and Goldberg D. 1990. The validity of Q estimates from borehole data using spectral ratios. *Geophysics* **55**, 97–101.

Shigapov R., Kashtan B., Droujinine A. and Mulder W. 2013. Methods for source-independent Q estimation from microseismic and crosswell perforation shot data in a layered, isotropic viscoelastic medium. SEG Technical Program Expanded Abstracts 2013 1014–1019.

Sun D., Jiao K., Cheng X., Vigh D. and Coates R. 2014. Source wavelet estimation in full waveform inversion. SEG Technical Program Expanded Abstracts 2014 1184–1188.

Tarantola A. 1984. Inversion of seismic reflection data in the acoustic approximation. *Geophysics* **49**, 1259–1266.

Tarantola A. 1988. Theoretical background for the inversion of seismic waveforms including elasticity and attenuation. *Pure and Applied Geophysics* **128**, 365–399.

Thomsen L. 1986. Weak elastic anisotropy. *Geophysics* **51**, 1954–1966.

Tromp J., Tape C. and Liu Q. 2005. Seismic tomography, adjoint methods, time reversal and banana-doughnut kernels. *Geophysical Journal International* **160**, 195–216.

Tsvankin I. 2012. *Seismic Signatures and Analysis of Reflection Data in Anisotropic Media*, 3rd edn. SEG.

Wang K., Krebs J.R., Hinkley D. and Baumstein A. 2009. Simultaneous full-waveform inversion for source wavelet and earth model, SEG Technical Program Expanded Abstracts 2009. 2537–2541.

Xue Z., Zhu T., Fomel S. and Sun J. 2016. Q-compensated full-waveform inversion using constant-Q wave equation: SEG Technical Program Expanded Abstracts, 1063–1068.

Zhang Q., Zhou H., Li Q., Chen H. and Wang J. 2016. Robust source-independent elastic full-waveform inversion in the time domain. *Geophysics* **81**, R29–R44.

Zhu T., Carcione J.M. and Harris J.M. 2013. Approximating constant-Q seismic propagation in the time domain. *Geophysical Prospecting* **61**, 931–940.

Zhu T., Harris J.M. and Biondi B. 2014. Q-compensated reverse-time migration. *Geophysics* **79**, S77–S87.

Zhu Y. and Tsvankin I. 2006. Plane-wave propagation in attenuative transversely isotropic media. *Geophysics* **71**, T17–T30.

Zhu Y., Tsvankin I., Dewangan P. and van Wijk K. 2006. Physical modeling and analysis of p-wave attenuation anisotropy in transversely isotropic media. *Geophysics* **72**, no. 1, D1–D7.

APPENDIX A: DERIVATION OF THE FIRST-ORDER ADJOINT SOURCE

The gradient of the 'source-independent' objective function (equations (10) and (11)) with respect to the model parameters can be written as

$$\frac{\partial F(\mathbf{m})}{\partial m} = \left[\frac{\partial \mathbf{u}}{\partial m} * \mathbf{d}^{\mathrm{ref}}\right]^T [\mathbf{u} * \mathbf{d}^{\mathrm{ref}} - \mathbf{d} * \mathbf{u}^{\mathrm{ref}}] - \left[\mathbf{d} * \frac{\partial \mathbf{u}^{\mathrm{ref}}}{\partial m}\right]^T [\mathbf{u} * \mathbf{d}^{\mathrm{ref}} - \mathbf{d} * \mathbf{u}^{\mathrm{ref}}]. \tag{A1}$$

The derivative $\partial \mathbf{u}^{\mathrm{ref}}/\partial m$ involves only the reference trace, which is often windowed to include just the direct P-arrival (especially for reflection data). Because usually the direct arrivals are weakly sensitive to the model parameters (i.e. $\partial \mathbf{u}^{\mathrm{ref}}/\partial m$ is small), this term can be ignored (see Choi and Alkhalifah 2011). Then equation (A1) becomes

$$\frac{\partial F(\mathbf{m})}{\partial m} = \left[\frac{\partial \mathbf{u}}{\partial m} * \mathbf{d}^{\mathrm{ref}}\right]^T [\mathbf{u} * \mathbf{d}^{\mathrm{ref}} - \mathbf{d} * \mathbf{u}^{\mathrm{ref}}] = \int_{-\infty}^{\infty} x(t) \int_{-\infty}^{\infty} \frac{\partial u}{\partial m}(t-\tau)\, d^{\mathrm{ref}}(\tau)\, d\tau\, dt, \tag{A2}$$

where summation over shots and receivers is implied and $\mathbf{x} = \mathbf{u} * \mathbf{d}^{\mathrm{ref}} - \mathbf{d} * \mathbf{u}^{\mathrm{ref}}$.

By introducing $\xi = t - \tau$ (so $\tau = t - \xi$), equation (A2) can be rewritten as

$$\begin{aligned}\frac{\partial F(\mathbf{m})}{\partial m} &= \int_{-\infty}^{\infty} x(t) \int_{-\infty}^{\infty} \frac{\partial u}{\partial m}(\xi)\, d^{\mathrm{ref}}(t-\xi)(-d\xi)dt \\ &= -\int_{-\infty}^{\infty} \frac{\partial u}{\partial m}(\xi)\left[\int_{-\infty}^{\infty} x(t)\, d^{\mathrm{ref}}(t-\xi)d\xi\right]dt \\ &= -\int_{-\infty}^{\infty} \frac{\partial u}{\partial m}(\xi)[d^{\mathrm{ref}} \otimes x](\xi)d\xi.\end{aligned} \tag{A3}$$

It is straightforward to show that $\mathbf{r} = \mathbf{d}^{\mathrm{ref}} \otimes \mathbf{x}$ (see equation (12)) can be treated as the adjoint source.

APPENDIX B: GRADIENTS FOR THE VISCOELASTIC PARAMETERS ΔC_{jklm}

In this appendix, we follow the approach of Charara, Barnes and Tarantola (2000) to derive the gradients of the objective function with respect to the stiffness differences ΔC_{jklm}. Applying the Born approximation to the momentum conservation law and using equation (3) yields

$$\delta f_i = \rho\, \delta \ddot{u}_i - \frac{\partial}{\partial x_j}\, \delta \sigma_{ij}, \tag{B1}$$

and

$$\delta T_{ij} = \delta \sigma_{ij} - C^U_{ijkl}\, \delta \epsilon_{kl} - \Delta C_{ijkl}\, \delta r_{kl}, \tag{B2}$$

where δu_i, $\delta \sigma_{ij}$, $\delta \epsilon_{kl}$ and δr_{kl} are the perturbed wavefield variables, and $\delta \mathbf{f}$ and $\delta \mathbf{T}$ are the 'virtual' force and stress determined by the perturbed model parameters ($\delta \rho$, δC^U_{ijkl} and $\delta \Delta C_{ijkl}$):

$$\delta f_i = -\ddot{u}_i\, \delta \rho, \tag{B3}$$

$$\delta T_{ij} = \epsilon_{kl}\, \delta C^U_{ijkl} + r_{kl}\, \delta \Delta C_{ijkl}. \tag{B4}$$

The solution of the perturbed viscoelastic wave equation has the form:

$$\begin{aligned}\delta u_i &= \int_V dV \int_0^T G_{ij}\,(\delta f_j)\,dt - \int_V dV \int_0^T \frac{\partial G_{ij}}{\partial x_k}\,(\delta T_{jk})\,dt \\ &= -\int_V dV \int_0^T G_{ij}\,(\delta\rho)\,\ddot{u}_j\,dt \\ &\quad -\int_V dV \int_0^T \frac{\partial G_{ij}}{\partial x_k}\left[(\delta C^U_{jklm})\,\epsilon_{lm} + (\delta\Delta C_{jklm})\,r_{lm}\right]dt,\end{aligned} \tag{B5}$$

where G_{ij} denotes the elastic Green's function.

Comparing equation (B5) with

$$\delta\mathbf{u} = \int_V \frac{\partial\mathbf{u}}{\partial\mathbf{m}}\,\delta\mathbf{m}\,dV, \tag{B6}$$

where $\partial\mathbf{u}/\partial\mathbf{m}$ denotes the Fréchet kernel (Tarantola, 1988), we obtain

$$\frac{\partial u_i}{\partial\Delta C_{jklm}} = -\int_0^T \frac{\partial G_{ij}}{\partial x_k}\,r_{lm}\,dt. \tag{B7}$$

The adjoint of the operator in equation B6 can be written as

$$\delta m = \sum_{\text{sources}} \int_0^T \left[\frac{\partial u_i}{\partial m}\right]^* \delta u_i\,dt, \tag{B8}$$

where the kernels $\partial u_i/\partial\mathbf{m}$ should be identical for a linear operator and its transpose (Tarantola 1988). Then the derivatives of the objective function F with respect to the viscoelastic parameters become

$$\begin{aligned}\frac{\partial F}{\partial\Delta C_{jklm}} \equiv \delta\Delta C_{jklm} &= \sum_{\text{sources}} \int_0^T \left[\frac{\partial u_i}{\partial\Delta C_{jklm}}\right]^* \delta u_i\,dt' \\ &= \sum_{\text{sources}} \int_0^T \left[\frac{\partial u_i}{\partial\Delta C_{jklm}}\right] \delta u_i\,dt' \\ &= -\sum_{\text{sources}} \int_0^T \int_0^T \frac{\partial G_{ij}}{\partial x_k}\,r_{lm}\,\delta u_i\,dt\,dt'.\end{aligned} \tag{B9}$$

By defining the adjoint wavefield as

$$u_j^\dagger = \int_0^T G_{ij}\,\delta u_i\,dt, \tag{B10}$$

we rewrite equation (B9) as

$$\frac{\partial F}{\partial\Delta C_{jklm}} \equiv \delta\Delta C_{jklm} = -\sum_{\text{sources}} \int_0^T \frac{\partial u_j^\dagger}{\partial x_k}\,r_{lm}\,dt. \tag{B11}$$

Therefore, the gradients for the viscoelastic parameters ΔC_{jklm} are the zero-lag cross-correlations of the adjoint strain fields $\partial u_j^\dagger/\partial x_k$ with the forward memory variables r_{lm} (Charara *et al.* 2000).